journal of the mechanical behavior of biomedical materials 103 (2020) 103595

Contents lists available at ScienceDirect

Journal of the Mechanical Behavior of Biomedical Materials

journal homepage: http://www.elsevier.com/locate/jmbbm

Cartilage and collagen mechanics under large-strain shear within *in vivo* and at supraphysiogical temperatures

Lauren Marshall [a], Anna Tarakanova [a,b], Phoebe Szarek [b], David M. Pierce [a,b,*]

[a] Department of Mechanical Engineering, University of Connecticut, 191 Auditorium Road, Unit 3139, Storrs, CT, 06269, USA
[b] Department of Biomedical Engineering, University of Connecticut, 260 Glenbrook Road, Unit 3247, Storrs, CT, 06269, USA

ARTICLE INFO

Keywords:
Articular Cartilage
Collagen
Large strain
Shear
Temperature
Denaturation

ABSTRACT

Human joints, particularly those of extremities, experience a significant range of temperatures *in vivo*. Joint temperature influences the mechanics of both joint and cartilage, and the mechanics of cartilage can affect the temperature of both joint and cartilage. Thermal treatments and tissue repairs, such as thermal chondroplasty, and *ex vivo* tissue engineering may also expose cartilage to supraphysiological temperatures. Furthermore, although cartilage undergoes principally compressive loads *in vivo*, shear strain plays a significant role at larger compressive strains. Thus, we aimed to determine whether and how the bulk mechanical responses of cartilage undergoing large-strain shear change (1) within the range of temperatures relevant *in vivo*, and (2) both during and after supraphysiological thermal treatments. We completed large-strain shear tests (10 and 15%) at four thermal conditions: 24°C and 40°C to span the *in vivo* range, and 70°C and 24°C repeated after 70°C to explore mechanics during and after potential treatments. We calculated the bulk mechanical responses (strain-energy dissipation densities, peak-to-peak shear stresses, and peak-effective shear moduli) as of function of temperature and used statistical methods to probe significant differences. To probe the mechanisms underlying differences we assessed specimens, principally the type II collagen, with imaging (second harmonic generation and transmission electron microscopies, and histology) and assessed the temperature-dependent mechanics of type II collagen molecules within cartilage using steered molecular dynamics simulations. Our results suggest that the bulk mechanical responses of cartilage depend significantly on temperature both within the *in vivo* range and at supraphysiological temperatures, showing significant reductions in all mechanical measures with increasing temperature. Using imaging and simulations we determined that one underlying mechanism explaining our results may be changes in the molecular deformation profiles of collagen molecules versus temperature, likely compounded at larger length scales. These new insights into the mechanics of cartilage and collagen may suggest new treatment targets for damaged or osteoarthritic cartilage.

1. Introduction

Human joints, particularly those of extremities, experience a significant range of temperatures *in vivo* (Horvath and Hollander, 1949; Becher et al., 2008; Ammer, 2012; Abdel-Sayed et al., 2014). Becher et al. (2008) directly recorded the temperatures within the knees of both alpine skiers and indoor joggers during exertion and found intra-articular temperatures varied from 24.4 – 38.8°C based on the external thermal environment. Synovial fluid within the knee joint also affects energy dissipation and heat transfer, and thus the intra-articular temperature and cartilage (Bali and Sharma, 2011; 10 Abdel-Sayed et al., 2014; Moghadam et al., 2015).

Articular cartilage is a soft tissue that covers the ends of bones within articulating joints. Joint temperature influences the mechanics of both joint and cartilage, and the mechanics of cartilage can affect the temperature of both joint and cartilage. Behrou et al. (2018) determined that temperature significantly influences the mechanical behavior of cartilage at early loading stages in confined and unconfined compression. Conversely, Moghadam et al. (2015) and Abdel-Sayed et al. (2014) showed that cyclic loading of cartilage increases the intra-articular temperature within the knee due to viscous energy dissipation.

Thermal treatments and tissue repairs, such as thermal chondroplasty (Anderson et al., 2019), and *ex vivo* tissue engineering (Wright and Humphrey, 2002; Sobol et al., 2011) may expose cartilage to

* Corresponding author. Department of Mechanical Engineering, University of Connecticut, 191 Auditorium Road, Unit 3139, Storrs, CT, 06269, USA.
E-mail address: dmpierce@engr.uconn.edu (D.M. Pierce).

https://doi.org/10.1016/j.jmbbm.2019.103595
Received 19 June 2019; Received in revised form 13 September 2019; Accepted 10 December 2019
Available online 17 December 2019

supraphysiological temperatures. New heating device technologies, such as powerful lasers and microwaves, generally propel these treatment advances rather than a deep understanding of the altered tissue mechanics in response to heating (Wright and Humphrey, 2002).

Although cartilage undergoes principally compressive loads *in vivo*, shear strain plays a significant role at larger compressive strains (Butz et al., 2011). Indeed, compression *in vivo* can generate shear strains greater than 10% (Chan et al., 2016). Shear in cartilage is also linked to chondrocyte death and secretion of proinflammatory factors (Athanasiou et al., 2016).

Cartilage comprises fluid and electrolytes (68-65% by wet weight), type II collagen fibers (10–25%), proteoglycans (5–10%), and chondrocytes (<4%) (Mow et al., 2005). Furthermore, the shear stiffness of cartilage originates principally from the dense network of type II collagen (Zhu et al., 1993). Temperature likely affects the mechanical response of these constituents individually, and the complex interplay of these constituents generates the remarkable mechanical responses of healthy cartilage.

Despite the variability in intra-articular (and thus cartilage) temperatures *in vivo*, and increasing interest in thermal-based treatments for cartilage, there is little information regarding the temperature-dependent bulk mechanical response of articular cartilage, particularly under large-strain shear. Furthermore, there is little information coupling temperature-dependent changes in bulk tissue mechanics to the underlying molecular mechanisms generating such changes. Thus there is a pressing need to quantify temperature-dependent changes to cartilage on both tissue and cellular/molecular scales to, e.g., more effectively identify and apply thermal treatments to donors.

Given that articular cartilage experiences a range of temperatures *in vivo* (Horvath and Hollander, 1949; Becher et al., 2008; Ammer, 2012; Abdel- Sayed et al., 2014) and during specialized thermal treatments (Wright and Humphrey, 2002; Sobol et al., 2011; Anderson et al., 2019), we aimed to determine whether and how the bulk mechanical responses of cartilage undergoing large-strain shear change (1) within the range of temperatures relevant *in vivo*, and (2) both during and after supraphysiological thermal treatments. We completed large-strain shear tests (10 and 15%) at four thermal conditions: 24°C and 40°C to span the *in vivo* range, and 70°C and 24°C repeated after 70°C to explore mechanics during and after potential treatments. We calculated the bulk mechanical responses (strain-energy dissipation densities, peak-to-peak shear stresses, and peak-effective shear moduli) as of functions of temperature and used statistical methods to probe significant differences. To probe the mechanisms underlying differences we assessed specimens, principally the type II collagen, with imaging (second harmonic generation (SHG) microscopy, transmission electron microscopy (TEM) microscopy, and histology) and assessed the temperature-dependent mechanics of type II collagen molecules within cartilage (via inter- and intra-molecular bonding analysis) using steered molecular dynamics (SMD) simulations.

2. Materials and methods

2.1. Specimen preparation

We harvested healthy cartilage (Musculoskeletal Transplant Foundation; first donor verified OARSI grade 0 via histology and donors verified visually thereafter) from both lateral and medial condyles of male and female donors (36.6 yrs ± 8.43, $n = 5$) (Pritzker et al., 2006). We first determined the local split-line direction (SLD) by pricking the articular surface of the cartilage with a dissecting needle dipped in India ink (Carballido-Gamio et al., 2008). Next we selected specimens from seven locations representing different loading conditions within the joint, cf. Maier et al. (2017). Within the patellofemoral groove we selected locations to be at the border to the condyle (B), and in the center (C) and lateral side (L) of the joint. Within the condyles we selected regions based on bearing load at different knee-flexion angles: 0° (L_0), 75° (L_{75}), and 120° (L_{120}); and one non-load-bearing region (N), cf. (Bingham et al., 2008; Maier et al., 2017).

We extracted 3×3 mm^2 full-thickness cuboid specimens using a square punch, ensuring one edge of the specimens remained parallel to the local SLD. We trimmed the bone surface parallel to the articular surface while leaving the cartilage-bone interface intact to ensure *in situ* boundary conditions for testing. We used a digital-precision caliper to measure the dimensions of the cuboid specimen, excluding subchondral bone, and averaged four measurements (accuracy of 0.01 mm). Finally, we submerged any specimens not tested immediately in Phosphate Buffered Saline (PBS) and stored them individually at −80°C (Athanasiou et al., 2009; Szarko et al., 2010). We present all donor data in Appendix A, Table A.1.

2.2. Triaxial shear test

We performed mechanical simple-shear tests in a temperature-controlled PBS bath using our triaxial shear-testing machine (Messphysik, Fürstenfeld, AT). We mounted specimens to two loading platens, one covered in fiberglass and one covered in ABS plastic, using cyanoacrylate gel (Loctite, Henkel AG & Co., Düsseldorf, DE; service temperature up to 82°C). The top platen rigidly connected to a three-axis load cell (K3D60, Me-Messsysteme, Henningsdorf, DE; 0.17 mN resolution, ≤ 0.2% linear error) mounted to a screw-driven crossbar (z-direction). The bottom platen connected to a biaxial translation stage (x-, y-direction), cf. . We monitored the temperature of the PBS bath with a temperature probe (Pt100-94, Omega, Norwalk, CT; Class-A, ±0.15°C) and controlled the temperature with a water heater (ECO Silver, Lauda-Brinkmann, Delran, NJ) with a feedback loop into the testing software.

First, we mounted the fluid-saturated specimens to the loading platens with cyanoacrylate gel and compressed them with 0.2 N force for 300 s, allowing the glue to dry. We then removed the compressive force and added PBS including antibiotics (100 U/ml penicillin and 100 mg/ml streptomycin) and protease inhibitors (Sigma Aldrich, St. Louis, MO) to prohibit degeneration. Once the PBS reached 24°C, we allowed the tissue to equilibriate for 2000 s to ensure fluid saturation and equilibrium (Boettcher et al., 2016). Then, we applied axial pre-compressions of 1% of the original specimen thicknesses and allowed specimens to rest for 3000 s. We applied simple-shear displacements at 75 μm/min parallel to the SLD for strain magnitudes of ±10% and ±15% and measured three orthogonal reaction forces and displacements in time (Maier et al., 2017, 2019a). After loading at both strain magnitudes at 24°C, we ramped the temperature of the PBS at 2°C/min to 40°C, repeated the loading profile, and repeated the process again at 70°C. Between loading at each strain magnitude and after each increase in temperature we zeroed the axial compressive forces for 3000 s and let the specimens reach equilibrium. For one specimen from each donor we repeated the loading profile again at 24°C immediately after ramping down from the 70°C loading.

2.3. Image-based assessments

For each image-based assessment we prepared three unloaded, pristine specimens using thermal treatments at 24°C, 40°C, and 70°C lasting the duration of the mechanical tests (approximately 4 h) and imaged as detailed below.

2.3.1. Second harmonic generation confocal microscopy

We performed SHG imaging (Zeiss LSM 510, Oberkochen, DE) using a tunable Ti: Sapphire laser (Coherent Chameleon, Santa Clara, CA) at 850 nm for excitation of the nonlinear signal. We acquired signals in non-descanned detection using a specialized filter (425 ± 13 nm bandpass filter; FF01-425/26–25, Semrock, Rochester, NY). We used a water-immersion objective (W Plan-Apochromat 20×/1.0) and a 600 × 600 μm (2480 × 2480 pixel) field of view. We keep the orientation SLD consistent across all images and imaged at depths of 80–120 μm from the

articular surface and through the thickness.

2.3.2. Transmission electron microscopy

After the specified thermal treatments we trimmed the bone and cut specimens into 0.5 mm-thick slices parallel to the SLD. We fixed specimens overnight in 3% glutaraldehyde, 3% paraformaldehyde, 0.05% w/v tannic acid in 0.1 M PIPES buffer using a protocol adapted from. We post-fixed with 1% osmium tetroxide for 1 h and *en bloc* stained with saturated 2% uranyl acetate in 50% ethanol for 15 min. We rinsed the specimens in buffer solution before placing them in 2.5% Reynold's lead citrate for 3 min. We dehydrated specimens in graded ethanol before clearing with propylene oxide. We infiltrated and embedded the specimens with Spurr's resin and polymerized the resin in a flat-bottom embedding capsule for 24 h at 70°C. We then cut 50 nm ultra-thin sections using a Diatome Ultra 45° diamond knife (Diatome US, Hatfield, PA) on a Leica Ultracut UCT ultramicrotome (Leica Biosystems Inc., Buffalo Grove, IL) and collected the 1–2 mm sections on copper 50-mesh grids.

We performed TEM imaging using a FEI Tecnai 12 G^2 Spirit BioTWIN transmission electron microscope (FEI Company, Hillsboro, OR) at 80 kV with a 4 megapixel 2k XR40 CCD camera (Advanced Microscopy Techniques, Woburn, MA). We imaged in the center 50% of each slice. Within each image we measured the diameters of greater than ten representative collagen fibrils at three points along each fibril using only the center-most 1130 × 1130 pixel regions of each image to preserve clarity. We calculated both the median fibril diameters and the percent changes in fibril diameters at each temperature. We used Fiji for ImageJ (National Institutes of Health, Bethesda, MD) for image processing (Schindelin et al., 2012; Rueden et al., 2017).

2.3.3. Histology

After the specified thermal treatments we decalcified the specimens in 0.5 M EDTA for one week. We embedded specimens in paraffin and sectioned at 6 μm. We stained the slides with either Safranin-O fast green (Novaultra Safranin-O stain kit, IHC World, Ellicott City, MD) or PicroSirius red (Novaultra Sirius red stain kit, IHC World) to probe qualitative changes to the proteoglycan and collagen fiber contents, respectively.

2.4. Data analyses

We calculated the shear strain and shear stress as $\gamma = \Delta l / L$ and $\tau = f/A$, respectively, where Δl is the applied displacement, L is the original thickness of the specimen, f is the measured force parallel to the SLD, and A is the cross-sectional area of the specimen. For statistical analyses we calculated the strain-energy dissipation density (E_{DI}) as

$$E_{DI} = \oint_{\gamma_{min}}^{\gamma_{max}} \tau d\gamma, \tag{1}$$

where γ_{min} and γ_{max} are the minimum and maximum shear strains of a loading cycle. We calculated the peak-to-peak shear stresses (τ_{PP}) by taking the difference between the maximum and minimum shear stresses as

$$\tau_{PP} = \tau(\gamma_{max}) - \tau(\gamma_{min}). \tag{2}$$

We also calculated the peak-effective shear modulus (G_{PE}) by finding the slopes of linear least-squares fits over 10 progressive data points along the stress-strain curves. For each magnitude of shear strain applied (±10%, ±15%), we calculated the positive and negative slopes as

$$G^+ = \frac{\tau_{avg}}{\gamma_{avg}}, \quad \text{for } \tau_{avg} \geq 0 \text{ and } \gamma_{avg} \geq 0, \tag{3}$$

$$G^- = \frac{\tau_{avg}}{\gamma_{avg}}, \quad \text{for } \tau_{avg} < 0 \text{ and } \gamma_{avg} < 0, \tag{4}$$

where τ_{avg} is the vertical projection of the best-fit line and γ_{avg} is the complementary horizontal projection. We then calculated G_{PE} by averaging G^+ and G^- at each strain magnitude (Santos et al., 2017; Maier et al., 2019a). We used MATLAB R2018a (MathWorks, Natick, MA) for all calculations.

2.5. Statistical analyses

We determined the minimum number of specimens ($n = 36$) using an *a priori* power analysis after 20 tests based on $\mu_1/\sigma = 0.95$ (80% significance, 83.2% power). Using our preliminary data, we estimated a difference in means of 0.397 mJ/mm^3 strain-energy dissipation density with a temperature increase from 24°C to 40°C, and with a standard deviation of 0.42 mJ/mm^3. We also performed a post-hoc power analysis to confirm sufficient power.

For each type of mechanical or morphological data we first checked for normality using a Shapiro-Wilk test. If one normality test failed we reported only medians and interquartile ranges $[Q_3, Q_1]$ for consistency. We then performed the Wilcox Rank-Sum tests to assess statistical significance in the mechanical responses and fibril diameters (measured via TEM) between pairs of temperatures. To probe inter- and intra-donor variability we used the Kruskal-Wallis test by ranks with donor (D1-5), anatomical position (medial or lateral condyle), and joint location (L1-7) as categorical variables. Following significant correlations we conducted post-hoc, Tukey tests to probe pair-wise groupings within categorical variables. We also assessed the influence of specimen thickness using Pearson's correlation coefficient r. We used SPSS Statistics 25 (IBM Corporation, Armonk, NY) with $p < 0.05$ for significance for all statistical analyses.

2.6. Molecular model and steered molecular dynamics simulations

We constructed a type II collagen-like sequence from UniProtKB - P02458 (CO2A1_HUMAN), using 60 amino acids, residue no. 201 to 260, of 1487 residues in type II collagen. We built a homogeneous tropocollagen model with the interactive Triple-Helical collagen Building Script (THe BuScr, ver. 1.07) (Rainey and Goh, 2004) resulting in a molecular segment of approximately 17 nm in length. To probe the effects of temperature on the mechanical behavior and unfolding pathway of collagen molecules, we performed steered molecular dynamics (SMD) simulations on these systems. We performed equilibration using the GROMACS 5.1.2 simulation package (Van Der Spoel et al., 2005) and steered molecular dynamics at 24°C, 40°C, and 70°C with the GROMOS96 54a7 force field and the single point charge (SPC) water model for solvent. See Appendix D for further details on the methods.

We conducted our SMD simulations at six pulling speeds: 100, 50, 10, 1, 0.5, 0.1 m/s for structures at a temperature of 70°C and identified a slow and fast pulling regime at a cutoff of 1 m/s: at or below a pulling rate of 1 m/s the mechanical response does not change significantly (Appendix D, Fig. D.11). Thus, we considered temperature effects on the mechanical response of collagen for slow rate deformation at 1 m/s. We then conducted a total of 18 molecular pulling simulations with six simulations at each temperature: 297 K (24°C), 313 K (40°C) and 343 K (70°C) and determined the averaged temperature-dependent force-strain profiles from each set of six simulations. We measure extension of the molecule as the total distance between the center of mass of the N-terminal Cα-atom in chain 1 and the center of mass of one C-terminal Cα-atom on chain 3. To correlate molecular mechanisms with bulk tissue responses we compared ratios of temperature-dependent changes in peak molecular forces to those in median peak-to-peak shear stresses, using the responses at 24°C as a benchmark. We used in-house TCL and Matlab scripts to perform all analysis. For all simulations, we used the Extreme Science and Engineering Discovery Environment (XSEDE).

3. Results

We performed a total of 216 shear tests using 36 healthy human cartilage specimens from five donors including both males and females. We show representative shear stress-strain plots in Fig. 1.

The Shapiro-Wilk test for normality revealed non-normal distributions for strain-energy dissipation density, peak-to-peak shear stresses, and peak-effective shear moduli. Therefore, we showed median and interquartile ranges for these parameters. The thicknesses of specimens showed a normal distribution (1.99 mm ± 0.432, M± SD).

3.1. Temperature-dependent mechanics

We show box plots of the complete mechanical data in Fig. 2.

The Wilcox rank sum test revealed significant differences in strain-energy dissipation densities, peak-to-peak shear stresses, and peak-effective shear moduli determined at all three testing temperatures and at both strain magnitudes. In the five repeated 24°C tests (after 70°C), strain-energy dissipation densities differed significantly from the initial 24°C test at both strain magnitudes ($p = 0.043$), but the peak-to-peak shear stresses and peak-effective shear moduli showed no significant differences.

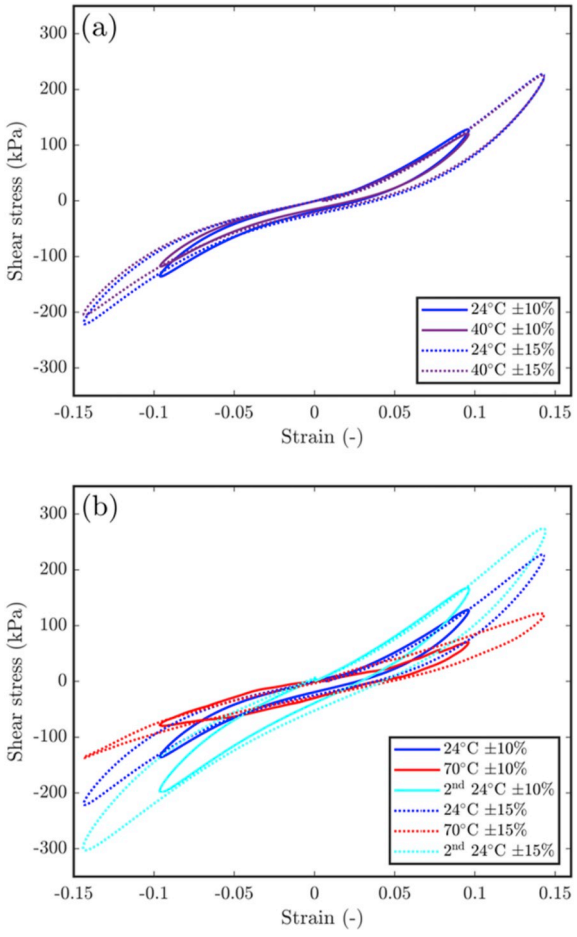

Fig. 1. Overall we observed nonlinear stress-strain relationships with distinct hystereses for both ±10 and ±15% applied bulk shear strain where stiffness, nonlinearity, and hysteresis generally reduced with increasing temperature. Representative shear stress-strain plots of healthy human cartilage at (a) 24°C and 40°C to span the *in vivo* temperature range, and (b) 70°C and 24°C repeated after 70°C to assess effects of supraphysiological temperatures.

3.2. Image-based assessments

3.2.1. Second harmonic generation microscopy

We show SHG images completed immediately after thermal treatments in Fig. 3.

We see no appreciable differences due to temperature and slight preferential alignment of the network of fibers corresponding to the superficial zone.

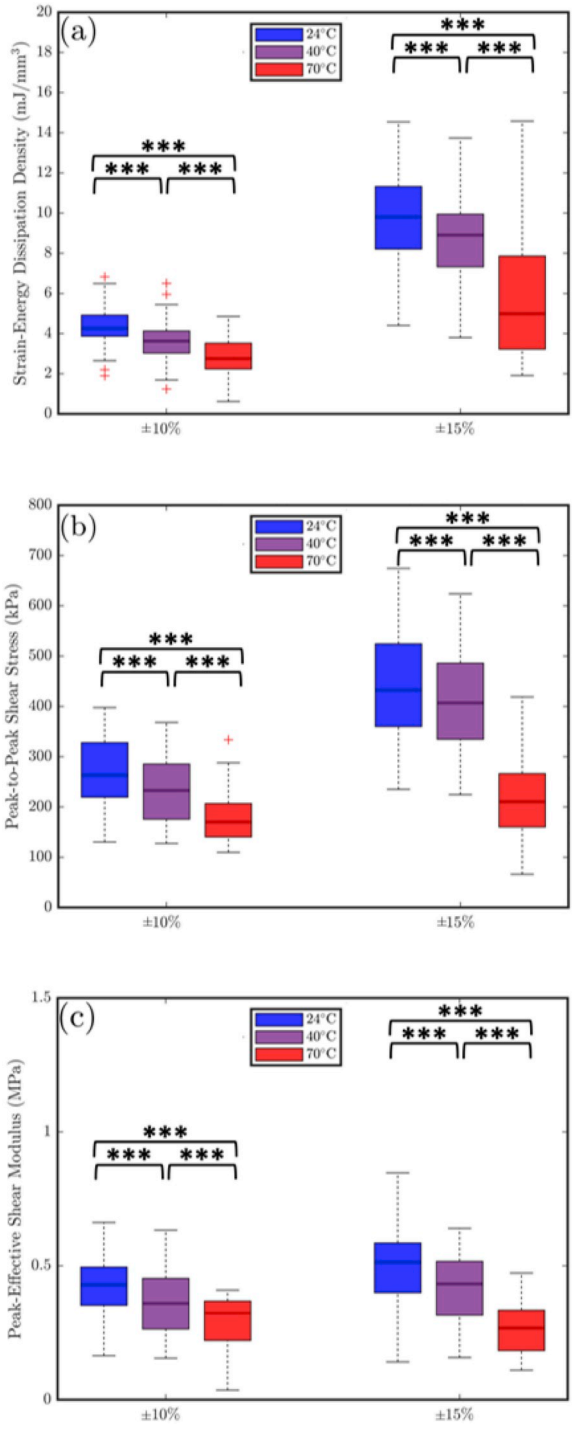

Fig. 2. (a) Strain-energy dissipation densities, (b) peak-to-peak shear stresses, and (c) peak-effective shear moduli decrease significantly with increasing temperature. Box plots show medians and interquartile ranges (boxes), maximum and minimum values (whiskers), and outliers (+) where *** indicates statistical significance $p < 0.001$.

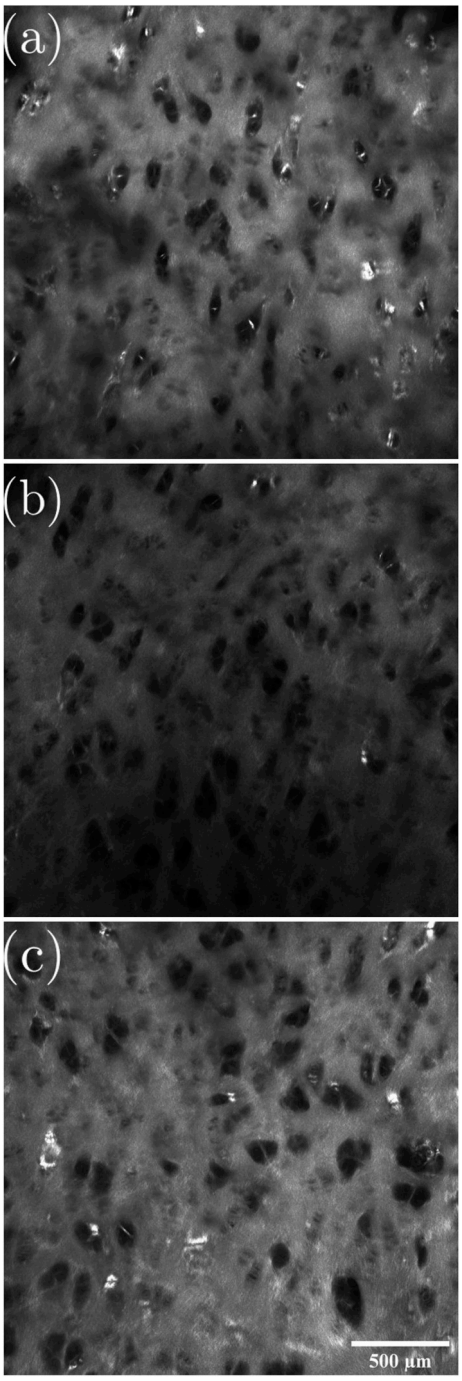

Fig. 3. SHG images completed after thermal treatments at (a) 24˚C, (b) 40˚C, (c) 70˚C for approximately 4 h showed no appreciable differences. The split-line direction aligns vertically in each image.

3.2.2. *Transmission electron microscopy*

We show TEM images completed immediately after thermal treatments in Fig. 4.

To quantify these insights, we show box plots of the fibril diameters by thermal treatments in Fig. 5.

Fibril diameters were not normally distributed. We determined medians and interquartile ranges of 72 nm [56, 81] at 24˚C, 91 nm [63, 106] at 40˚C (22.8% increase), and 106 nm [84, 121] at 70˚C (38.2% increase).

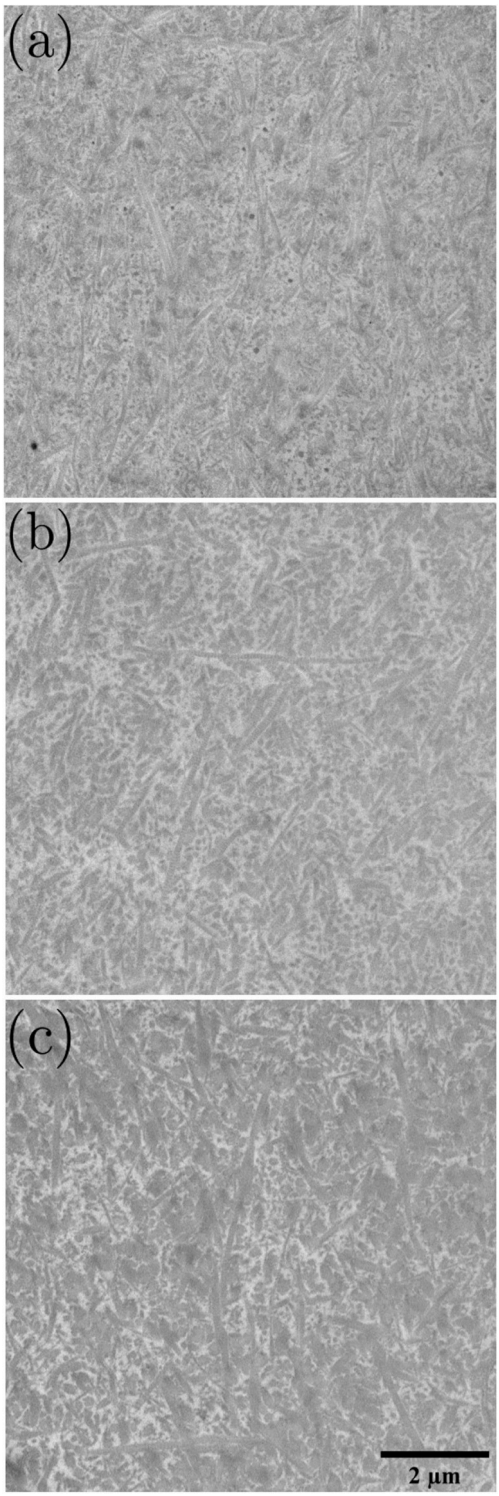

Fig. 4. Transmission electron microscopy images reveal significant fibril swelling after thermal treatments at (a) 24˚C, (b) 40˚C, and (c) 70˚C.

3.2.3. *Histology*

Histological images completed after thermal treatments showed no appreciable differences and we show slides stained with both Safranin-O fast green and PicroSirius red in Appendix B, Fig. B.8 and B.9.

3.3. *Intra- and inter-donor variabilities*

The Kruskal-Wallis test by ranks revealed significant differences in

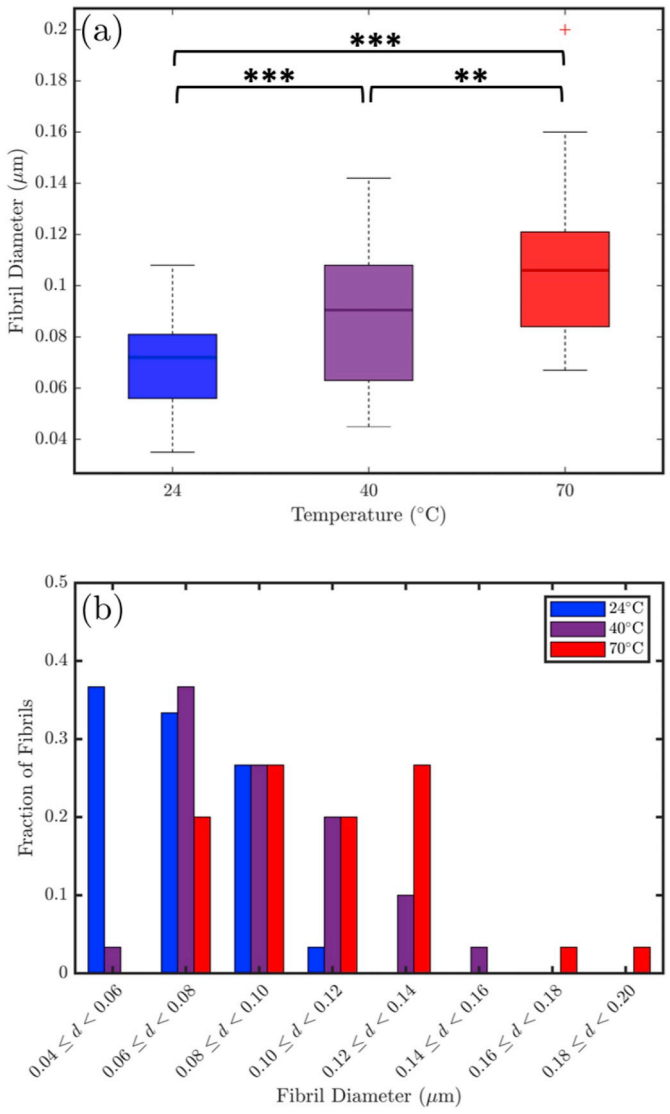

Fig. 5. Fibril diameter increases significantly after increasing the magnitude of thermal treatments, presented as (a) a box plot of fibril diameters (** indicates statistical significance $p < 0.01$ and *** indicates $p < 0.001$) and (b) a histogram of fibril diameters.

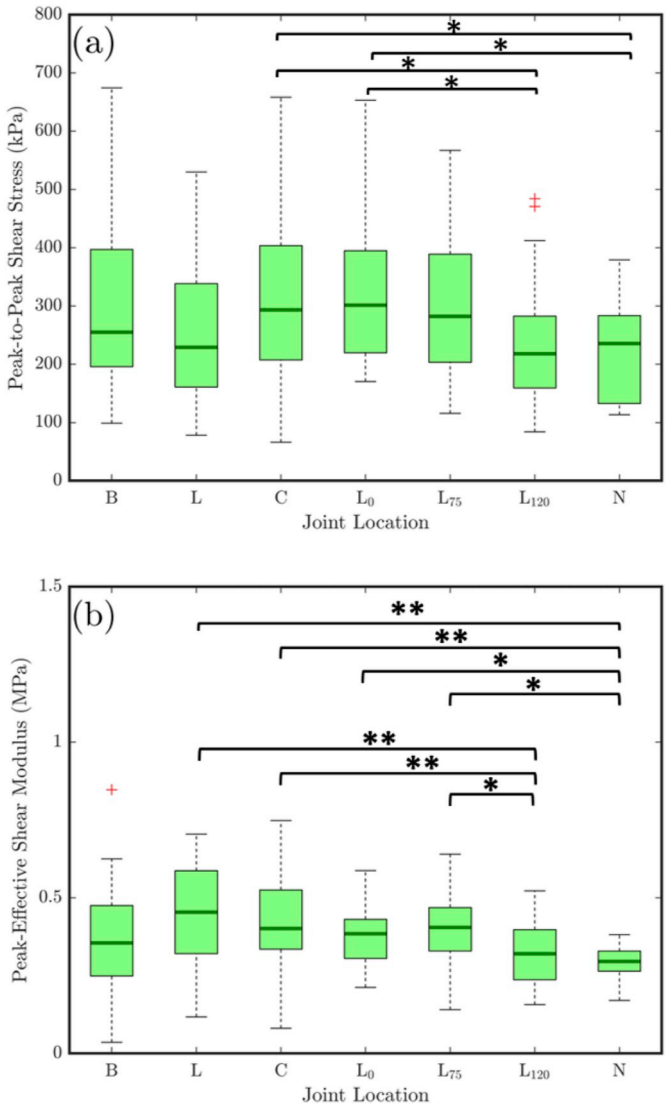

Fig. 6. (a) Peak-to-peak shear stresses and (b) peak-effective shear moduli vary significantly among intra-condyle joint locations. We determined significance based on the combined response calculated from both strain magnitudes (10% and 15%) where * corresponds to $p < 0.05$ and ** to $p < 0.01$.

mechanical responses among donors, joint locations, and anatomical positions. The donors median mechanical responses were 4.58 mJ/mm^3 [3.38, 8.38] ($p = 0.04$), 255 kPa [191, 376] ($p = 0.06$), and 0.368 MPa [0.276, 0.474] ($p = 0.02$) (median plus interquartile range) for the strain-energy dissipation densities, peak-to-peak shear stresses, and peak-effective shear moduli respectively. The lateral condyle was significantly stiffer than the medial condyle ($\approx$ 15%) when measured by peak-effective shear modulus, 0.397 MPa [0.276, 0.503] in the lateral condyle versus 0.340 MPa [0.275, 0.407] in the medial condyle. We show box plots of the significant differences in mechanical responses among joint locations in Fig. 6.

The Tukey test revealed specimens from the load-bearing region at 120° knee flexion and the meniscus-covered region (L_{120} and N) were less stiff (when measured by peak-to-peak shear stress) than specimens from the center of the patellofemoral groove and the load-bearing region at 0° knee flexion (C and L_0). When measured by peak-effective shear modulus, specimens from the meniscus-covered region were less stiff than those from the 0° and 75° knee flexion regions (L_{75}) and the center and lateral side of the patellofemoral groove (L). Additionally, specimens from the 120° knee flexion angle region were less stiff than those from the 75° knee flexion angle and the lateral side and center of the patellofemoral groove.

We found no significant differences in the measured thicknesses of the specimens among donors ($p = 0.560$) or among the joint locations we studied ($p = 0.231$). All three mechanical parameters vary significantly with specimen thickness and we present the linear best fits in Appendix C, Fig. C.10.

3.4. Molecular model and simulations

We show the force-strain profiles at each temperature determined as an average of six pulls in Fig. 7 (a), overlaid with a polynomial fit. Two deformation regimes characterized molecular extension: (1) unwinding in tensile stretch as strands rotated, and (2) slipping in shear (strand 3 against strands 1 and 2). We observed lower forces in the slipping regime at higher temperatures. We also show the persistence of protein-water hydrogen bonds through the deformation in Fig. 7(b). Formation of protein-water hydrogen bonds increased in the slipping regime at all temperatures. Fewer protein-water hydrogen bonds persisted at higher temperatures in both regimes. Finally, we show snapshots of the

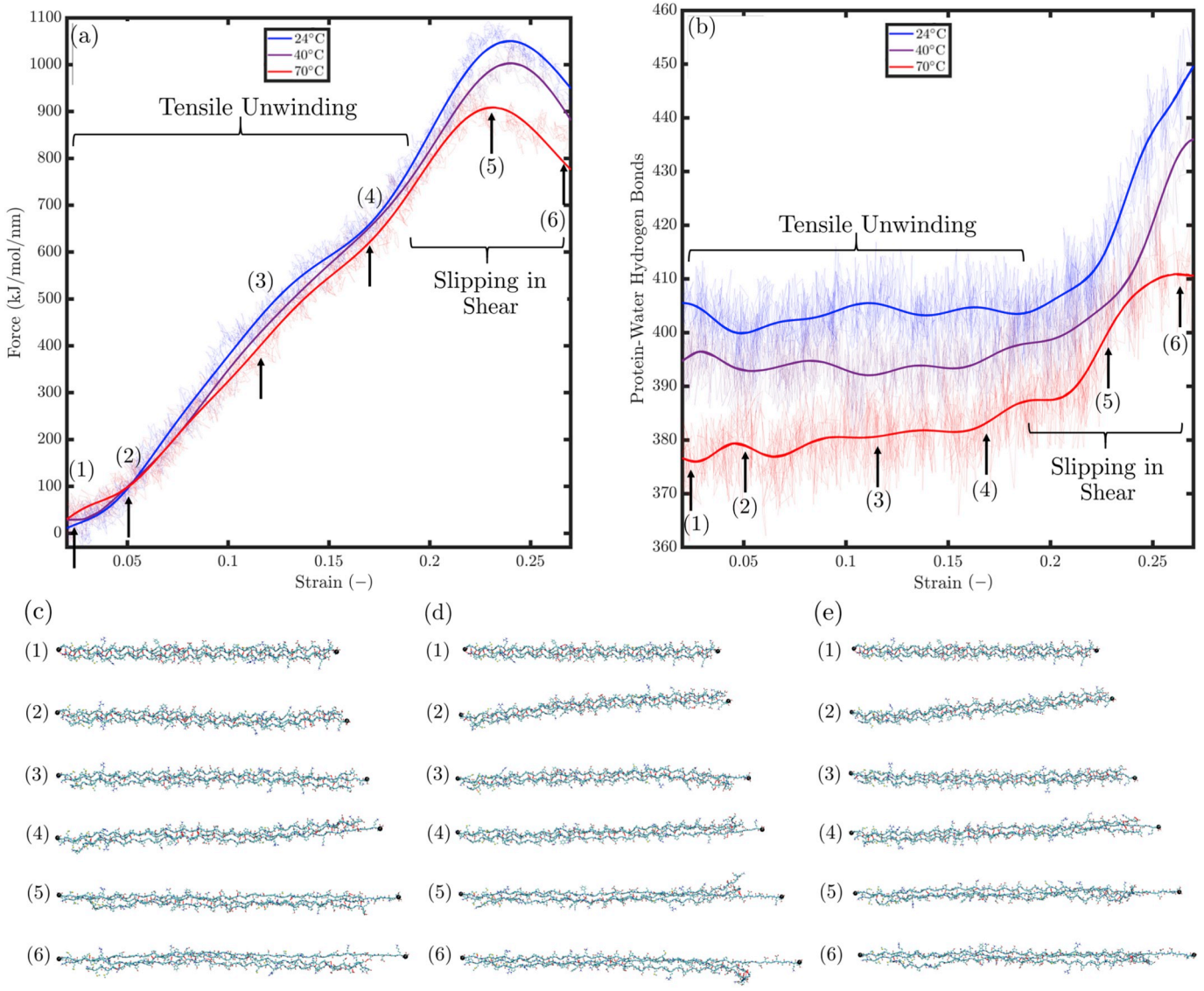

Fig. 7. We observed two regimes in collagen deformation with the prescribed load: first, tensile unwinding, then shear slip as strand 3 slides along strands 1 and 2. Protein-water hydrogen bonds increase as the strands unwind and slip. We observed a sharp increase in the number of hydrogen bonds formed between protein and water molecules particularly in the slipping regime as strand 3 is sheared along strands 1 and 2. The stability of hydrogen bonds decreases with increasing temperature, which results in significant differences in shear force during the slipping regime. (a) Average force-strain profiles of collagen type II molecule, and (b) average hydrogen bond profiles both where the solid lines represent polynomial best fits to the averaged response from six simulations each at 24°C, 40°C, and 70°C. Deformation states at (c) 24°C, (d) 40°C, and (e) 70°C at six strains: (1) 0%, (2) 5%, (3) 12%, (4) 17%, (5) 23%, (6) 27%.

deformation at six strains 0%, 5%, 12%, 17%, 23%, and 27% (numbered 1 through 6, respectively) for 24°C, 40°C, and 70°C in Fig. 7(c–e), respectively.

We calculated peak molecular forces of 1051 kJ/mol/nm, 1003 kJ/mol/nm, and 909 kJ/mol/nm at 24°C, 40°C, and 70°C, respectively. Regarding the ratios of temperature-dependent changes in mechanical responses, the ratio of molecular forces for 40°C/24°C was 1003.3/1050.5 = 0.955, while this was (232/263 = 0.884, 7.4% difference) for bulk stresses at 10% bulk shear strain and (406/432 = 0.941, 1.4% difference) at 15% bulk shear strain. Making the same comparison for 70°C/24°C the ratio of molecular forces was 908/1050.5 = 0.865, while this was (170/263 = 0.646, 25% difference) for bulk stresses at 10% bulk shear strain and (210/432 = 0.486, 44% difference) at 15% bulk shear strain.

4. Discussion

We were the first to probe the temperature dependence of human articular cartilage under large shear strains (up to 15%) in the *in vivo* and supraphysiological temperature ranges. We aimed to measure only the response of the solid constituents (collagens and proteoglycans) and thus we applied shear-strain deformations at a relatively slow rate of 75 μm/min to ensure fluid-pressure independent, quasi-static loading (Maier et al., 2017). Similar experiments tested human cartilage at *in vivo* and supraphysiological temperatures in compression (June and Fyhrie, 2010) and cyclic loading (Abdel-Sayed et al., 2014). Cartilage specimens underwent two freeze-thaw cycles, which should not alter mechanical responses (Szarko et al., 2010).

Our results (Fig. 1) show a nonlinear stress-strain relationship with distinct hysteresis for all temperatures at both strain magnitudes. This hysteresis is characteristic of collagen fibers, the main load-bearing component of human articular cartilage under shear (Zhu et al., 1993; Silverberg et al., 2014; Griffin et al., 2014). The nonlinearities near the loading peaks result from progressive stiffening of networked collagen fibers at larger shear strains (Buckley et al., 2008; Zopf et al., 2015).

4.1. Temperature-dependent mechanics

Our statistical analyses revealed significant differences in strain-energy dissipation within the *in vivo* range where increasing temperature results in decreasing energy dissipation. The optimal temperature for production of extracellular matrix (particularly collagen) by chondrocytes lies between 32˚C and 37˚C (Peltonen et al., 1980; Ito et al., 2014). Following, the intrinsic energy dissipation of cartilage may present a sufficient means to maintain the human knee undergoing cyclic loading (e.g., walking) at a temperature optimal for homeostasis.

Increasing temperature also resulted in reduced peak-to-peak shear stresses and peak-effective shear moduli within the *in vivo* range. Thus increasing temperature indicates a reduced recruitment of collagen, perhaps due to disruption of the fibers or of the stabilizing cross-linkages. Our results contradict June and Fyhrie (2010), who found supraphysiological temperature (60˚C) produced a stiffer mechanical response versus 24˚C. We attribute this discrepancy to their dynamic loading which includes contributions from fluid pressure that we neglected with our quasi-static test. Rate-dependent loads also tend to reduce collagen recruitment (Mow et al., 2005), which may also contribute to the discrepancy.

During supraphysiological temperatures, cartilage presents significantly lower resistance to shear loading. This change may result from both hydrolysis of hydrogen bonds and thermal denaturation of proteoglycans which create weaker collagen-proteoglycan interactions thus reducing stiffness in shear (Hardingham, 1981; Sobol et al., 1999; Mow et al., 2005).

When we retested cartilage at 24˚C after exposure to 70˚C, cartilage largely recovered its mechanical response, but dissipated significantly more strain energy in shearing (Fig. 1(b)). After heating to 70˚C hydrogen bonds cannot effectively re-form and cartilage is less able to re-hydrate, thus explaining the increase in strain-energy dissipation (Chen et al., 1997; Pearson and Espino, 2013; Fields et al., 2017). The hydration-dependent mechanical response, combined with the hydrolysis and partial recovery of bonds surrounding the collagen triple helix at high temperatures, may also explain the significant difference in strain-energy dissipation density between the first 24˚C loading and the 24˚C repeated after exposure to 70˚C.

4.2. Image-based assessments

4.2.1. Second harmonic generation confocal microscopy

Researchers previously applied SHG microscopy to detect thermal denaturation of collagen fibers via a loss of birefringence (Thomsen et al., 1989; Kim et al., 2000; Wright and Humphrey, 2002; Chen et al., 2012; Lilledahl et al., 2015). Yet we did not find qualitative changes in the intensity of our SHG signal after thermal treatment at 70˚C (Fig. 3(c)). This discrepancy likely results from different kinetic reaction pathways that drive the denaturation rates, as laser heating common in the literature introduces additional thermomechanical damage from rapidly-induced pressure gradients (Sankaran and Walsh, 1998).

4.2.2. Transmission electron microscopy

We did find thermally induced swelling of collagen fibrils at 40˚C and 70˚C (a 22.8% and 38.2% increase from 24˚C, respectively) (Fig. 4), a clear indication of damage (Barr et al., 1987; Tang et al., 1997; Whittaker et al., 2000). Interpreting this result and in light of the SHG images, we appeared to thermally damage the collagen fibrils but not fully denature the collagen fiber bundles (Tang et al., 1997; Mow et al., 2005).

4.2.3. Histology

Histological images completed after thermal treatments showed no appreciable differences. The images with PicroSirius-Red staining (Fig. B.9) did show loss of color intensity after 70˚C treatment, but only in the deep zone nearest the bone interface. The result is consistent with Lin et al. (2006) who admit histology is not the best indicator of tissue denaturation.

4.3. Intra- and inter-donor variabilities

We selected male and female donors within a relatively narrow age range. The significant differences among donors may result from differences in the number of available explants (Appendix A), e.g., we were only able to excise and test four explants from donor 2 due to relatively low stiffness and poor bone-tissue adhesion.

We found the lateral condyle was ≈ 15% stiffer (by peak-effective shear modulus) than the medial condyle. The result agrees with Lyyra et al. (1995), who showed that the lateral condyle can be up to 30% stiffer than the medial condyle. However, while some researchers report significant differences in the mechanical responses between condyles (Berteau et al., 2016; Santos et al., 2017; Jurvelin et al., 2000), others report no significant differences (Mow et al., 1989; Athanasiou et al., 1991; Williamson et al., 2003; Deneweth et al., 2015).

To probe differences in the mechanical responses among joint locations we selected locations that experience different magnitudes of loading *in vivo* while ensuring specimen thicknesses between 1 and 3 mm (Carballido-Gamio et al., 2008; Salzmann et al., 2011). We grouped strain and temperature magnitudes together for the statistical analyses presented in Fig. 6. However, similar statistical analyses on these data separated by strain magnitude, we found no statistically significant differences by joint location likely indicating that different locations within the joint respond to changes in temperature similarly. We found that explants from the patellofemoral groove were stiffer than those from the condyles by both peak-to-peak shear stresses and peak-effective shear moduli. Franz et al. (2001) reported that cartilage from the patellofemoral groove is softer than that from the condyles while Athanasiou et al. (1991) reported the opposite.

4.4. Molecular model and simulations

We performed pulling simulations at 24˚C, 40˚C, and 70˚C on models of collagen type II – representative of the dominant solid, load-bearing molecular component of articular cartilage – to probe molecular mechanisms underlying the temperature-dependent changes we observed at the bulk tissue scale (Fig. 7(a)). To simulate shear-like deformations, we fixed two strands at one end by constraining the center of mass of the two N-terminal Cα-atoms, while we pulled the third strand at the C-terminal end Cα-atom. Molecular unwinding characterized the initial deformation regime as the three strands rotate about one another. Thereafter we observed slipping of the strands (as chain 3 was drawn out against chains 1 and 2) characterized by progressively lower forces with increasing temperature, from 24˚C to 40˚C–70˚C.

The differences we observed in the force-strain profiles versus temperature correlated to the presence of protein-water hydrogen bonds as we loaded the molecules (Fig. 7(b)). While the number of intramolecular hydrogen bonds remained similar at all temperatures, fewer hydrogen bonds formed between the protein and water solvent at higher temperatures. While the triple helical structure of the collagen molecule stabilized intramolecular hydrogen bonds, faster dynamics at higher temperatures disrupted protein-solvent hydrogen bonds more readily, resulting in smoother extension and lower required forces to achieve strand slipping. While the presence of protein-solvent hydrogen bonds results in oscillation of the three strands of the collagen molecule through the slipping regime at lower temperatures, we observed smoother, more cohesive slip at 70˚C (Fig. 7(c–e) at 24˚C, 40˚C, and 70˚C, respectively). Our results suggest that temperature-dependent changes in the bulk response of cartilage may stem from the particulars of hydrogen bond persistence around collagen molecules, effects that may be compounded by the hierarchical structure of collagen fibers networked within cartilage.

Additionally, temperature-dependent reductions in peak molecular

forces mirror corresponding reductions in median peak-to-peak shear stresses within the range of *in vivo* temperatures (1%–7% difference), but show only moderate correspondence at supraphysiological temperatures (25%–44% difference) where additional mechanisms likely become important.

4.5. Limitations and outlook

The frequency of our large-strain shearing was not physiological (much less than 1 Hz), and we did not consider the mechanical contributions of fluid pressure. The magnitudes of shear strain we report are averaged shear displacements within our specimens. Since cartilage is heterogeneous through the thickness the depth-dependent strain will similarly vary through the thickness, as reported in both compression (Schinagl et al., 1997; Wang et al., 2002; Gannon et al., 2015) and shear (Wong et al., 2008; Buckley et al., 2008; Motavalli et al., 2014; Maier et al., 2019b).

Both TEM and histological imaging required extended specimen preparation involving several days of fixation at room temperature which may induce changes in thermal damage prior to imaging. Thus, our TEM and histological images may not reveal the full extent of thermal damage. We could, however, control the temperature of the specimens during SHG microscopy.

Our results suggest that full understanding of cartilage mechanics requires large-strain analyses accounting for the range of temperatures relevant *in vivo*, and depending on the application, supraphysiological temperatures. Understanding the roles of joint and cartilage temperature in cartilage mechanics and in disease progression could reveal new treatment targets for osteoarthritis and other rheumatic diseases. Abdel-Sayed et al. (2014) demonstrated that osteoarthritic cartilage presents a reduced ability to dissipate energy, which may change joint temperature and cell homeostasis. Finally, tracking the role of temperature in long-term joint and cartilage performance may have implications for disease onset in athletes and workers in extreme climates.

Acknowledgements

This material is based upon work supported by the National Science Foundation under Grant No. 1653358. This work utilized the Extreme Science and Engineering Discovery Environment (XSEDE) (Towns et al., 2014), which is supported by the National Science Foundation under Grant No. ACI-1053575. XSEDE resourced Stampede 2 and Ranch (Texas Advanced Computing Center) and Comet (San Diego Supercomputing Center) through allocation TG-MCB180008. We performed parts of this work at the Biosciences Electron Microscopy Facility at the University of Connecticut. We thank Franz Maier for help with mechanical testing, Stephany Santos for help with SHG microscopy, and Hicham Drissi and the Musculoskeletal Transplant Foundation for providing human tissues. We also thank the Statistical Consulting Service at the University of Connecticut for help with statistical analyses.

Appendix E. Supplementary data

Supplementary data to this article can be found online at https://doi.org/10.1016/j.jmbbm.2019.103595.

Appendix A. Donor Data

Table A.1
Donor data with age in years and specimen dimensions x (split-line direction), y, and t (thickness) in mm. Sex specifies male or female (M/F), Knee specifies left or right (L/R), and Condyle specifies medial or lateral (M/L).

Donor	Specimen	Age	Sex	Knee	Condyle	x	y	t
1	1–01	37	F	L	L	3.03	2.84	2.44
1	1–02	37	F	L	L	2.94	3.03	1.67
1	1–03	37	F	L	L	3.00	2.89	1.72
1	1–04	37	F	L	L	2.87	2.76	1.95
1	1–05	37	F	L	L	2.94	3.01	2.05
1	1–06	37	F	L	L	2.96	2.94	1.86
1	1–07	37	F	L	L	3.01	3.01	1.62
1	1–08	37	F	L	L	2.98	2.97	1.90
2	2–01	45	M	L	M	2.95	2.98	2.37
2	2–02	45	M	L	M	2.94	3.06	2.13
2	2–03	45	M	L	M	2.98	2.95	1.78
2	2–04	45	M	L	M	3.08	3.01	2.63
3	3–01	37	F	R	L	2.89	2.96	1.75
3	3–02	37	F	R	L	3.13	2.99	2.35
3	3–03	37	F	R	L	2.96	3.02	2.22
3	3–04	37	F	R	L	2.79	2.94	1.98
3	3–05	37	F	R	L	2.98	3.01	1.79
3	3–06	37	F	R	L	2.84	3.12	1.93
3	3–07	37	F	R	L	3.07	3.02	1.82
4	4–01	21	F	L	L	3.00	3.10	2.04
4	4–02	21	F	L	L	2.93	2.96	3.25
4	4–03	21	F	L	L	2.92	3.06	0.8
4	4–04	21	F	L	L	2.97	3.01	1.84
4	4–05	21	F	L	L	2.95	3.06	1.96
4	4–06	21	F	L	L	3.05	3.07	2.09
4	4–07	21	F	L	L	3.01	3.02	1.56
4	4–08	21	F	L	L	2.92	2.95	2.60
4	4–09	21	F	L	L	3.01	3.03	2.17
4	4–10	21	F	L	L	2.99	2.91	2.09
5	5–01	43	M	R	M	3.02	3.35	1.96
5	5–02	43	M	R	M	3.02	2.94	1.98

(*continued on next page*)

Table A.1 (*continued*)

Donor	Specimen	Age	Sex	Knee	Condyle	*x*	*y*	*t*
5	5–03	43	M	R	M	2.99	3.03	2.19
5	5–04	43	M	R	M	3.04	3.12	1.11
5	5–05	43	M	R	M	3.01	3.14	1.36
5	5–06	43	M	R	M	3.01	2.98	1.92
5	5–07	43	M	R	M	3.05	2.95	2.24
5	5–08	43	M	R	M	3.08	2.96	2.41

Appendix B. Histology

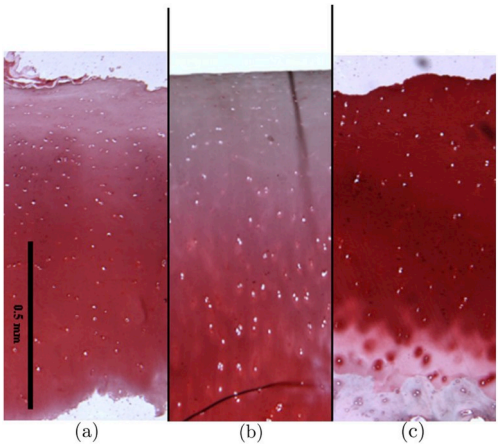

Fig. B.8. Images of Safranin-O-stained histological slices of cartilage heat-treated at (a) 24°C, (b) 40°C, and (c) 70°C.

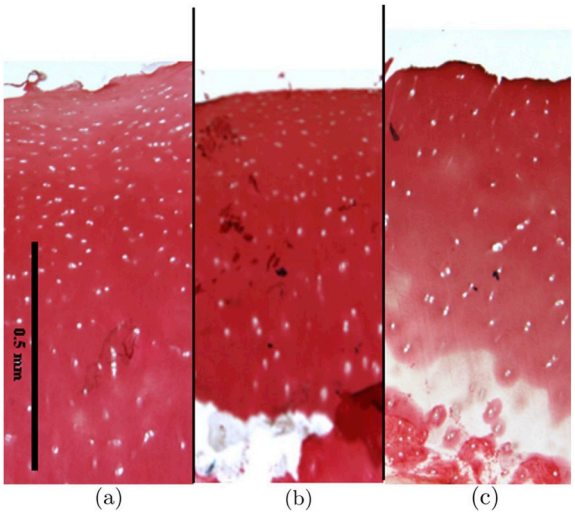

Fig. B.9. Images of PicroSirius Red-stained histological slices of cartilage heat-treated at (a) 24°C, (b) 40°C, and (c) 70°C.

Appendix C. Effects of Specimen Thicknesses

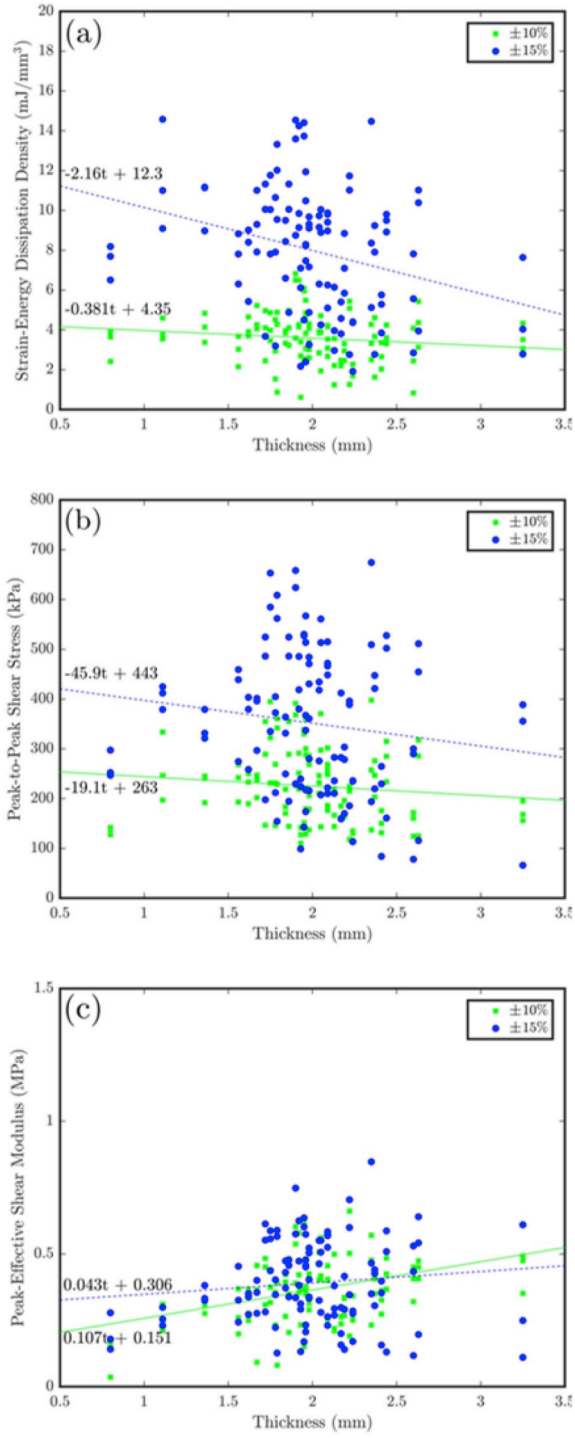

Fig. C.10. Linear fits for bulk mechanical responses as functions of specimen thicknesses show moderate correlations. (a) Strain-energy dissipation density (at 10% applied bulk shear strain $R^2 = 0.23$, at 15% $R^2 = 0.30$), (b) peak-to-peak shear stress (10% $R^2 = 0.26$, 15% $R^2 = 0.42$), and (c) peak-effective shear modulus (10% $R^2 = 0.23$, 15% $R^2 = 0.43$).

Appendix D. Details on the Molecular Dynamics Simulations of Collagen

In single amino acid letter code, the sequence used is GPMGPMGPRGPPGPAGAPGPQGFQGNPGEPGEPGVSGPMGPRGPPGPPGKPGDDGEAGKP. First, we generated the collagen molecule backbone structure with THe BuScr. Then, we added side chains to the backbone structure using the BuScr and Scwrl4 package. We mutated hydroxylated prolines into hydroxyproline and amalgamated the full atomistic collagen molecule structure via the HypScwrl2. tcl script through the BuScr package, resulting in a tropocollagen molecular segment of approximately 17 nm in length.

In each case, we fully solvated the molecule in a SPC water box (Berendsen et al., 1984) 30 × 6 × 6 nm in size and neutralized by adding counter

ions. We chose the GROMOS 54A7 force field (Schmid et al., 2011) to simulate collagen-like peptides (Lorenzo and Caffarena, 2005; Gautieri et al., 2009;

Tang et al., 2018). We constrained covalent bond lengths involving hydrogen with the SETTLE and LINCS algorithms (Hess, 2007). We used a time step of 2 fs and calculated long-range electrostatic interactions using the fourth order Particle-Mesh Ewald sums (PME) method (Essmann et al., 1995). We computed non-bonded interactions with a cutoff distance of 1.4 nm and applied periodic boundary conditions to every dimension.

We used the steepest descent algorithm to minimize the systems and to eliminate steric clashes within the molecule. Next, we equilibrated solvent around the protein, while fixing the protein, through two equilibration stages, each 100 ps in length, with a time step of 1 fs. The first stage equilibrated in an NVT ensemble to stabilize temperature, while the second stage equilibrated in an NPT ensemble to stabilize system pressure. After the solvent equilibrated, we removed the protein restraint and equilibrated the protein and solvent in an NVT ensemble for an additional 15 ns. We used the Berendsen thermostat with a coupling constant of 1 ps for temperature coupling and the Parrinello-Rahman barostat with a coupling constant of 2 ps for pressure coupling.

We performed all SMD simulations in an NVT ensemble, with each system coupled to a heat bath at 297 K (24°C), 313 K (40°C), and 343 K (70°C) respectively via the Berendsen thermostat with a coupling constant of 1 ps. To perform SMD simulations, we linked via a virtual spring with an elastic constant of 1000 kJ $mol^{-1}nm^{-2}$ the center of mass of the two N-terminal Cα-atoms in chains 1 and 2, and the center of mass of one C-terminal Cα-atom on the remaining chain. The virtual spring extended along the longitudinal direction of the molecule. We used a time step of 2 fs in all SMD simulations.

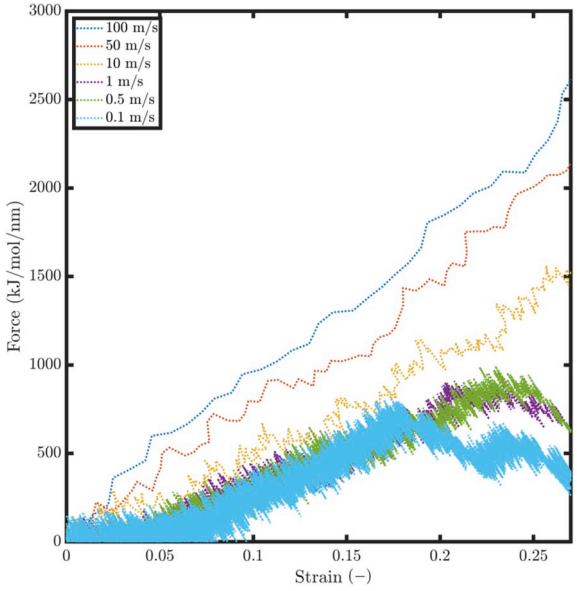

Fig. D.11. When pulling collagen at a rate of 1 m/s or lower the force response at 70°C does not change significantly and thus we chose to perform our steered molecular dynamics simulations at 1 m/s to preserve stable deformation behavior and improve computational expediency. Force-strain profiles for extension of collagen at 70°C for six pulling speeds: 100, 50, 10, 1, 0.5, and 0.1 m/s.

References

Abdel-Sayed, P., Moghadam, M.N., Salomir, R., Tchernin, D., Pioletti, D.P., 2014. Intrinsic viscoelasticity increases temperature in knee cartilage under physiological loading. J. Mech. Behav. Biomed. Mater. 30, 123–130.

Ammer, K., 2012. Temperature of the human knee: a review. Thermol. Int. 22, 131–151.

Anderson, S., Faucett, S., Flanigan, D., Gmabardella, R.A., Amin, N.H., 2019. The history of radiofrequency energy and Coblation in arthroscopy: a current concepts review of its application in chondroplasty of the knee. J. Exp. Orthop. 6, 1.

Athanasiou, K.A., Darling, E.M., Hu, J.C., 2009. Articular Cartilage Tissue Engineering, vol. 1. Morgan & Claypool Publishers, San Rafael, CA.

Athanasiou, K.A., Darling, E.M., Hu, J.C., 2016. Articular cartilage tissue engineering. In: Synth. Lect. Tissue Eng.

Athanasiou, K.A., Rosenwasser, M.P., Buckwalter, J.A., Malinin, T.I., Mow, V.C., 1991. Interspecies comparisons of in situ intrinsic mechanical properties of distal femoral cartilage. J. Orthop. Res. 9, 330–340.

Bali, R., Sharma, S.K., 2011. A model for intra-articular heat exchange in a knee joint. Tribol. Lett. 41, 379–386.

Barr, H., Tralau, C.J., Boulos, P.B., MacRobert, A.J., Tilly, R., Bown, S.G., 1987. The contrasting mechanisms of colonic collagen damage between photodynamic therapy and thermal injury. Photochem. Photobiol. 46, 795–800.

Becher, C., Springer, J., Feil, S., Cerulli, G., Paessler, H.H., 2008. Intra-articular temperature of the knee in sports - an in-vivo study of jogging and alpine skiing. BMC Muscoskelet. Disord. 9, 46.

Behrou, R., Foroughi, H., Haghpanah, F., 2018. Numerical study of temperature effects on the poro-viscoelastic behavior of articular cartilage. J. Mech. Behav. Biomed. Mater. 78, 214–223.

Berendsen, H.J.C., Postma, J.P.M., van Gunsteren, W.F., DiNola, A., Haak, J.R., 1984. Molecular dynamics with coupling to an external bath. J. Chem. Phys. 81.

Berteau, J.P., Oyen, M., Shefelbine, S.J., 2016. Permeability and shear modulus of articular cartilage in growing mice. Biomechanics Model. Mechanobiol. 15, 205–212.

Bingham, J.T., Papannagari, R., Van de Velde, S.K., Gross, C., Gill, T.J., Felson, D.T., Rubash, H.E., Li, G., 2008. In vivo cartilage contact deformation in the healthy human tibiofemoral joint. Rheumatology 47, 1622–1627.

Boettcher, K., Kienle, S., Nachtsheim, J., Burgkart, R., Hugel, T., Lieleg, O., 2016. The structure and mechanical properties of articular cartilage are highly resilient towards transient dehydration. Acta Biomater. 29, 180–187.

Buckley, M.R., Gleghorn, J.P., Bonassar, L.J., Cohen, I., 2008. Mapping the depth dependence of shear properties in articular cartilage. J. Biomech. 41, 2430–2437.

Butz, K.D., Chan, D.D., Nauman, E.A., Neu, C.P., 2011. Stress distributions and material properties determined in articular cartilage from MRI-based finite strains. J. Biomech. 44 (15), 2667–2672.

Carballido-Gamio, J., Bauer, J.S., Stahl, R., Lee, K.-Y., Krause, S., Link, T.M., Majumdar, S., 2008. Inter-subject comparison of MRI knee cartilage thickness. Med. Image Anal. 12, 120–135.

Chan, D.D., Cai, L., Butz, K.D., Trippel, S.B., Nauman, E.A., Neu, C.P., 2016. *In vivo* articular cartilage deformation: noninvasive quantification of intratissue strain during joint contact in the human knee. Sci. Rep. 6, 19220.

Chen, S.S., Wright, N.T., Humphrey, J.D., 1997. Heat-induced changes in the mechanics of a collagenous tissue: isothermal free shrinkage. J. Biomech. Eng. 119, 372–378.

Chen, X., Nadiarynkh, O., Plotnikov, S., Campagnola, P.J., 2012. Second harmonic generation microscopy for quantitative analysis of collagen fibrillar structure. Nat. Protoc. 7, 654–669.

Deneweth, J.M., Arruda, E.M., McLean, S.G., 2015. Hyperelastic modeling of location-dependent human distal femoral cartilage mechanics. Int. J. Non-Linear Mech. 68, 146–156.

Essmann, U., Perera, L., Berkowitz, M.L., Darden, T., Lee, H., Pedersen, L.G., 1995. A smooth particle mesh Ewald method. J. Chem. Phys. 103.

Fields, M., Spencer, N., Dudhia, J., McMillan, P.F., 2017. Structural changes in cartilage and collagen studied by high temperature Raman spectroscopy. Biopolymers 107, 1–8.
Franz, T., Hasler, E.M., Hagg, R., Weiler, C., Jakob, R.P., Mainil-Varlet, P., 2001. In situ compressive stiffness, biochemical composition, and structural integrity of articular cartilage of the human knee joint. Osteoarthr. Cartil. 9, 582–592.
Gannon, A.R., Nagel, T., Bell, A.P., Avery, N.C., Kelly, D.J., January, 2015. Postnatal changes to the mechanical properties of articular cartilage are driven by the evolution of its collagen network. Eur. Cells Mater. 29, 105–123.
Gautieri, A., Buehler, M.J., Redaelli, A., 2009. Deformation rate controls elasticity and unfolding pathway of single tropocollagen molecules. J. Mech. Behav. Biomed. Mater. 2.
Griffin, D.J., Vicari, J., Buckley, M.R., Silverberg, J.L., Cohen, I., Bonassar, L.J., 2014. Effects of enzymatic treatments on the depth-dependent viscoelastic shear properties of articular cartilage. J. Orthop. Res. 32, 1652–1657.
Hardingham, T.E., 1981. Proteoglycans: their structure, interactions and molecular organization in cartilage. Biochem. Soc. Trans. 9, 489–497.
Hess, B., 2007. P-LINCS: A Parallel Linear Constraint Solver for Molecular Simulation.
Horvath, S.M., Hollander, J.L., 1949. Intra-articular temperature as a measure of joint reaction. J. Clin. Investig. 28, 469–473.
Ito, A., Aoyama, T., Iijima, H., Nagai, M., Yamaguchi, S., Tajino, J., Zhang, X., Akiyama, H., Kuroki, H., 2014. Optimum temperature for extracellular matrix production by articular chondrocytes. Int. J. Hyperth. 30, 96–101.
June, R.K., Fyhrie, D.P., 2010. Temperature effects in articular cartilage biomechanics. J. Exp. Biol. 213, 3934–3940.
Jurvelin, J.S., Arokoski, J.P.A., Hunziker, E.B., Helminen, H.J., 2000. Topographical variation of the elastic properties of articular cartilage in the canine knee. J. Biomech. 33, 669–675.
Kim, B.M., Eichler, J., Reiser, K.M., Rubenchik, A.M., Da Silva, L.B., 2000. Collagen structure and nonlinear susceptibility: effects of heat, glycation, and enzymatic cleavage on second harmonic signal intensity. LSM 27, 329–335.
Lilledahl, M., Olderøy, M., Finnøy, A., Olstad, K., Brinchman, J.E., 2015. Second Harmonic Generation Imaging in Tissue Engineering and Cartilage Pathologies, vol. 9329, p. 93291C.
Lin, S.-J., Lo, W., Tan, H.-Y., Chan, J.-Y., Chen, W.-L., Wang, S.-H., Sun, Y., Lin, W.-C., Chen, J.-S., Hsu, C.-J., Tjiu, J.-W., Yu, H.-S., Jee, S.-., Dong, C.-Y., 2006. Prediction of heat-induced collagen shrinkage by use of second harmonic generation microscopy. J. Biomed. Opt. 11.
Lorenzo, A.C., Caffarena, E.R., 2005. Elastic properties, Young's modulus determination and structural stability of the tropocollagen molecule: a computational study by steered molecular dynamics. J. Biomech. 38.
Lyyra, T., Jurvelin, J., Pitkänen, P., Väätäinen, U., Kiviranta, I., 1995. Indentation instrument for the measurement of cartilage stiffness under arthroscopic control. Med. Eng. Phys. 17, 395–399.
Maier, F., Lewis, C.G., Pierce, D.M., 2019. The evolving large-strain shear responses of progressively osteoarthritic human cartilage. Osteoarthr. Cartil. 27, 810–822.
Maier, F., Lewis, C.G., Pierce, D.M., 2019. Through-thickness Patterns of Shear Strain Evolve in Early Osteoarthritis. Osteoarthritis CartilageIn press.
Maier, F.S., Drissi, H., Pierce, D.M., 2017. Shear deformations of human articular cartilage: certain mechanical anisotropies apparent at large but not small shear strains. J. Mech. Behav. Biomed. Mater. 65, 53–65.
Moghadam, M.N., Abdel-Sayed, P., Camine, V.M., Pioletti, D.P., 2015. Impact of synovial fluid flow on temperature regulation in knee cartilage. J. Biomech. 48, 370–374.
Motavalli, M., Akkus, O., Mansour, J.M., 2014. Depth-dependent shear behavior of bovine articular cartilage: relationship to structure. J. Anat. 225, 519–526.
Mow, V.C., Gibbs, M.C., Lai, W.M., Zhu, W.B., Athanasiou, K.A., 1989. Biphasic indentation of articular cartilage-II. A numerical algorithm and an experimental study. J. Biomech. 22, 853–861.
Mow, V.C., Gu, W.Y., Chen, F.H., 2005. Structure and function of articular cartilage and meniscus. In: Mow, V.C., Huiskes, R. (Eds.), Basic Orthopaedic Biomechanics & Mechano-Biology, third ed. Lippincott Williams & Wilkins, Philadelphia, pp. 181–258.
Pearson, B., Espino, D.M., 2013. Effect of hydration on the frequency-dependent viscoelastic properties of articular cartilage. Proc. Inst. Mech. Eng. H. 227, 1246–1252.
Peltonen, L., Palotie, A., Hayashi, T., Prockop, D.J., 1980. Thermal stability of type I and type III procollagens from normal human fibroblasts and from a patient with osteogenesis imperfecta. Proc. Natl. Acad. Sci. U.S.A. 77, 162–166.
Pritzker, K.P.H., Gay, S., Jimenez, S.A., Ostergaard, K., Pelletier, J.-P., Revell, P.A., Salter, D., van den Berg, W.B., 2006. Osteoarthritis cartilage histopathology: grading and staging. Osteoarthr. Cartil. 14, 13–29.
Rainey, J.K., Goh, M.C., 2004. An interactive triple-helical collagen builder. Bioinformatics 20.
Rueden, C.T., Schindelin, J., Hiner, M.C., DeZonia, B.E., Walter, A.E., Arena, E.T., Eliceiri, K.W., 2017. ImageJ2: ImageJ for the next generation of scientific image data. BMC Bioinf. 18, 529.
Salzmann, G.M., Buchberger, M.S., Stoddart, M.J., Grad, S., Milz, S., Niemyer, P., Sudkamp, N.P., Imhoff, A.B., Alini, M., 2011. Varying regional topology within knee articular chondrocytes under simulated in vivo conditions. Tissue Eng. A 17, 451–461.
Sankaran, V., Walsh, J.T., 1998. Birefringence measurement of rapid structural changes during collagen denaturation. Photochem. Photobiol. 68, 846–851.
Santos, S., Maier, F., Pierce, D.M., 2017. Anisotropy and inter-condyle heterogeneity of cartilage under large-strain shear. J. Biomech. 52, 74–82.
Schinagl, R.M., Gurskis, D., Chen, A.C., Sah, R.L., 1997. Depth-dependent confined compression modulus of full-thickness bovine articular cartilage. J. Orthop. Res. 15, 499–506.
Schindelin, J., Arganda-Carreras, I., Frise, E., 2012. Fiji: an open-source platform for biological-image analysis. Nat. Methods 9, 676–682.
Schmid, N., Eichenberger, A.P., Choutko, A., Riniker, S., Winger, M., Mark, A.E., van Gunsteren, W.F., 2011. Definition and testing of the GROMOS force-field versions 54A7 and 54B7. Eur. Biophys. 40.
Silverberg, J.L., Barrett, A.R., Das, M., Petersen, P.B., Bonassar, L.J., Cohen, I., 2014. Structure-function relations and rigidity percolation in the shear properties of articular cartilage. Biophys. J. 107, 1721–1730.
Sobol, E., Shekhter, A., Guller, A., Baum, O., Baskov, A., 2011. Laser-induced regeneration of cartilage. J. Biomed. Opt. 16.
Sobol, E.N., Kitai, M.S., Jones, N., Sviridov, A.P., Milner, T., Wong, B.J.F., 1999. Heating and structural alterations in cartilage under laser radiation. IEEE J. Quantum Electron. 35, 532–539.
Szarko, M., Muldrew, K., Bertram, J.E.A., 2010. Freeze-thaw treatment effects on the dynamic mechanical properties of articular cartilage. BMC Muscoskelet. Disord. 11, 1–8.
Tang, J., Godlewski, G., Rouy, S., Delacrétaz, G., 1997. Morphologic changes in collagen fibers after 830 nm diode laser welding. Lasers Surg. Med. 21, 438–443.
Tang, M., Li, T., Pickering, E., Gandhi, N.S., Burrage, K., Gu, Y.T., 2018. Steered molecular dynamics characterization of the elastic modulus and deformation mechanisms of single natural tropocollagen molecules. J. Mech. Behav. Biomed. Mater. 86.
Thomsen, S., Pearce, J.A., Cheong, W.F., 1989. Changes in birefringence as markers of thermal damage in tissues. IEEE Trans. Biomed. Eng. 36, 1174–1179.
Towns, J., Cockerill, T., Dahan, M., Foster, I., Gaither, K., Grimshaw, A., Hazlewood, V., Lathrop, S., Lifka, D., Peterson, G.D., Roskies, R., Scott, J.R., Wilkins-Diehr, N., 2014. XSEDE: accelerating scientific Discovery. Comput. Sci. Eng. 16.
Van Der Spoel, D., Lindahl, E., Hess, B., Groenhof, G., Mark, A.E., Berendsen, H.J.C., 2005. GROMACS: fast, flexible, and free. J. Comput. Chem. 26.
Wang, C.C., Deng, J.M., Ateshian, G.A., Hung, C.T., 2002. An automated approach for direct measurement of two-dimensional strain distributions within articular cartilage under unconfined compression. J. Biomech. Eng. 124, 557–567.
Whittaker, P., Zheng, S.-m., Patterson, M.J., Kloner, R.A., Daly, K.E., Hartman, R.A., 2000. Histologic signatures of thermal injury: applications in transmyocardial laser revascularization and radiofrequency ablation. Lasers Surg. Med. 27, 305–318.
Williamson, A.K., Chen, A.C., Masuda, K., Thonar, E.J., Sah, R.L., 2003. Tensile mechanical properties of bovine articular cartilage: variations with growth and relationships to collagen network components. J. Orthop. Res. 21, 872–880.
Wong, B.L., Bae, W.C., Chun, J., Gratz, K.R., Lotz, M., Sah, R.L., 2008. Biomechanics of cartilage articulation: effects of lubrication and degeneration on shear deformation. Arthritis Rheum. 58, 2065–2074.
Wright, N.T., Humphrey, J.D., 2002. Denaturation of collagen via heating: an irreversible rate process. Annu. Rev. Biomed. Eng. 4, 109–128.
Zhu, W.B., Mow, V.C., Koob, T.J., Eyre, D.R., 1993. Viscoelastic shear properties of articular cartilage and the effects of glycosidase treatments. J. Orthop. Res. 11, 771–781.
Zopf, D.A., Flanagan, C.L., Nasser, H.B., Mitsak, A.G., Huq, F.S., Rajendran, V., Green, G. E., Hollister, S.J., 2015. Biomechanical evaluation of human and porcine articular cartilage. The Laryngoscope 125, E262–E268.